Data-Driven Screening of Pivotal Subunits in Edge-Anchored Single Atom Catalysts for Oxygen Reactions

Qitong Ye,[‡,a] Xingxing Yi,[‡,a] Cai-Zhuang Wang,[b] Tao Zhang,[c] Yipu Liu,[a,*] Shiwei Lin[a,*] and Hong Jin Fan[c,*]

[a] *School of Materials Science and Engineering, Key Laboratory of Pico Electron Microscopy of Hainan Province, Hainan University, Haikou 570228 P. R. China*

[b] *Department of Physics and Astronomy, Iowa State University, Ames, IA 50011, USA*

[c] *School of Physical and Mathematical Sciences, Nanyang Technological University, 21 Nanyang Link, Singapore 637371, Singapore*

‡ *These authors have contributed equally to this work.*

* *Corresponding author. E-mail address: liuyp@hainanu.edu.cn; linsw@hainanu.edu.cn; fanhj@ntu.edu.sg*

Abstract

Oxygen reduction reaction (ORR) and the oxygen evolution reaction (OER) are key reactions in diverse energy conversion devices, highlighting the importance of efficient catalysts. Edge-anchored single atom catalysts (E-SACs) emerge as a special class of atomic structure, but the detailed configuration and its correlation with catalytic activity remain little explored. Herein, a total of 78 E-SACs (E-TM-N_x-C) have been constructed based on 26 transition metal (TM) species with three coordination patterns. Using structural stability and ORR/OER catalytic activity as the evaluation criteria, a few catalytic structures comparable to Pt (111) for ORR and IrO_2 (110) for OER are screened based on high-throughput calculations. The screening results unveil that the E-Rh-N_4-C configuration exhibits most efficient bifunctional activity for both ORR and OER with an overpotential of 0.38 and 0.61 V, respectively. Electronic structure analysis confirms the distinctive edge effects on the electronic properties of TM and N species, and the feature importance derived from machine learning illustrates the efficacy of E-TM-N_x subunit configuration in determining the catalytic activity of E-SACs. Finally, our trained Gradient Boosting Regression (GBR) model can accurately predict the OH intermediates adsorption strength for E-SACs, thereby paving the way for expanding catalytic structures based on E-SACs.

Keywords: Edge-anchored single-atom catalysts; Data-driven screening; high-throughput calculations; machine learning; oxygen reaction.

1. Introduction

The development of sustainable technologies and catalysts for efficient energy conversion reactions becomes increasingly urgent to fulfil the demand of earth sustainability and urban resilience.[1] Proton exchange membrane fuel cells (PEMFCs),[2] metal-air batteries,[3] and regenerative fuel cells are promising sustainable technologies, in which the chemical reactions are driven by catalysts.[4] In particular, the oxygen reduction reaction (ORR) and oxygen evolution reaction (OER) are most common reactions in these devices, with ORR serving as the cathode reaction in fuel cells and OER as the anode reaction in electrolyzers.[5] Additionally, for aqueous metal-air batteries and regenerative fuel cells, both ORR and OER catalysis are required at the same electrode.[6] As ORR and OER are reverse reactions with the 4-electron transfer process, they both exhibit low reaction kinetics.[7] Moreover, catalysts that can accelerate ORR generally have poor OER activity, and vice versa.[8-9] Currently, commercial ORR and OER catalysts mainly rely on precious metal materials such as Pt and IrO_2, and Pt-Ir-Ru alloys always exhibit bifunctional catalytic activity. However, the limited abundance and high cost of the precious metals restrict their larger-scale applications, which motivates researchers to develop new materials to reduce the usage of precious metals.[10-13] Single-atom catalysts (SACs) are considered to be one of the promising catalytic structures, which can dramatically reduce the loading of precious metals with high atomic utilization efficiency, leading to enhanced intrinsic activity for active sites. Consequently, it is promising for designing ORR/OER catalytic structures based on SAC configurations.[14-18]

Among the currently reported SACs, transition metal (TM) atoms are primarily anchored on the basal plane of substrate.[19-22] However, considering that metal species are dispersed at the atomic level in SACs, in principle they can anchor any defect sites of the support surface. Due to the presence of unsaturated dangling bonds and sp^2 hybridized C structures, TM atoms anchored at the graphene edge sites may exhibit significantly different electronic structures from the basal plane, leading to exceptional catalytic activities.[23-30] For instance, Zhang et al. decorated isolated Ru atoms onto the edge-rich carbon matrix, which exhibits remarkable HER activity (9.6 times mass activity that of commercial Pt/C-20% at 100 mV). This work highlights the contribution of the edges on carbon support in providing specific electronic field for Ru SAs.[26] Tian et al. synthesized series of Co-SACs with different edge-to-bulk ratios, and elucidated the importance of edge structures in modulating the electronic structure of Co atom and determining the ORR

pathways. Accordingly, the edge-rich Co-N/HPC catalyst achieved a superior H_2O_2 production rate (1.72 $molh^{-1}g_{cat}^{-1}$) with nearly 95% selectivity.[27] Moreover, Xiao et al. developed a self-sacrificed templating approach to prepare FeN_4 edge sites on graphitic nanosheets (Fe/N-G-SAC), which showed outstanding catalytic performance for both ORR and OER.[28] The calculations based on first-principles density functional theory (DFT) demonstrate that Fe atom would go through both intensified electron transfer and significant spin polarization at the edge site, leading to optimized adsorption behavior. This Fe/N-G-SAC catalyst was applied in Zn-air battery prototype, which operates with a narrow charge-discharge gap of 0.78 V. These prior experimental studies illustrate that, rational design of edge-anchored single atom catalysts (E-SACs) can enrich the SAC configurations and improve the catalytic performance. However, the current research on E-SACs is limited to specific E-SAC, and a systematic exploration for various transition metals is lacking. Data-driven screening via high-throughput calculation will allow for more efficient comparison of the structural characteristics and intrinsic activities among different E-SACs, leading to fast identification of catalysts to guide experimental synthesis.[31]

Herein, a total of 78 E-SACs are constructed with different coordination patterns between TM atoms and nitrogen species (denoted as E-TM-N_x-C). A set of thermodynamically and electrochemically stable E-TM-N_x-C are first screened out based on high-throughput DFT calculations. Their intrinsic ORR/OER activities and selectivities are then evaluated, and the most active and stable E-TM-N_x-Cs are carefully identified under ORR/OER conditions. Additional electronic structure analysis reveals unique role of the edge sites on the degree of electron transfer between TM and N species, leading to optimized modulation for the adsorption strength of the intermediates. Such a combined effect among TM SAs, N patterns and edge sites in catalytic activities for E-SACs is corroborated by machine learning (ML), demonstrating a clear structure-activity relationship of E-SACs. We also validate our trained GBR model for predicting the adsorption strength of involved intermediates during oxygen electrocatalysis based on existing E-SAC configurations.

2. Results and Discussion

2.1. Structural models and stabilities of E-TM-N_x-C

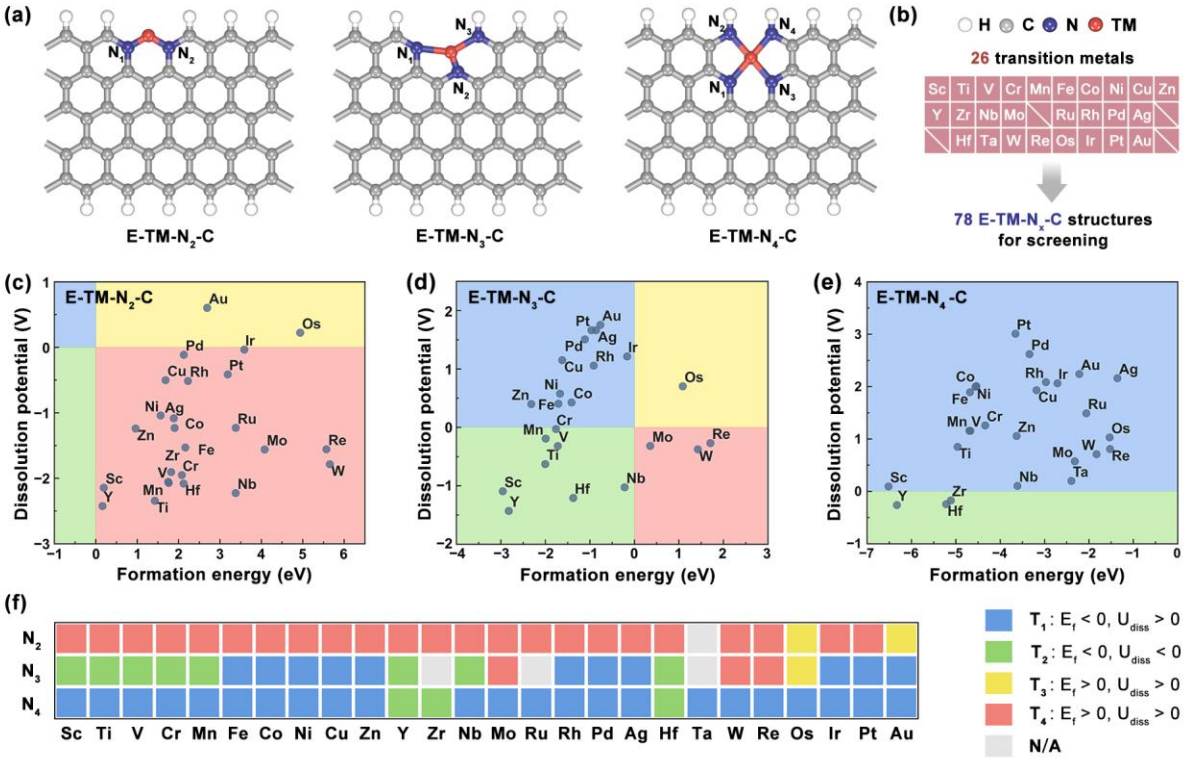

Figure 1. Type of edge-anchored single atom structures and stability screening. (a) Schematics of E-TM-N_2-C, E-TM-N_3-C and E-TM-N_4-C. (b) 26 transition metal atoms considered in this study, leading to 78 E-TM-N_x-C candidates. The calculated E_f and U_{diss} for (c) E–TM-N_2-C, (d) E-TM-N_3-C and (e) E-TM-N_4-C. The negative E_f together with positive U_{diss} (blue region) correspond to good stability. (f) Stability classification of E-TM-N_x-C based on E_f and U_{diss}. Four different categories (T_1, T_2, T_3, T_4) are depicted using different colors. The gray color denotes the non-convergent (N/A) structures.

Models of edge-anchored single atom catalysts are constructed based on previous experimental reports.[27,30] Specifically, the graphene nanoribbon structure is chosen to simulate the edge of graphene layers, and the width of the graphene nanoribbon is optimized to be 8.55 Å. The single atom (SA) is intentionally anchored around the unsaturated C sites of graphene nanoribbon, and other dangling bonds for C species are terminated by H atoms.[27,32] Considering different anchoring sites for SA and typical SA structures (TM-N_x, TM denote transition metal) reported so far,[33] three types of TM-SA-N_x configurations with 2-4 TM-N coordination numbers are investigated in this work, namely, E-TM-N_2-C, E-TM-N_3-C and E-TM-N_4-C (Figure 1a). In

E-TM-N_2-C, the SA substitutes one of the six membered carbon rings at the edge of graphene nanoribbon, and two adjacent C atoms are substituted by N species to form SA-N_2 structure. As for E-TM-N_3-C and E-TM-N_4-C, C atoms at edge are removed to construct SA-N_3 structure and SA-N_4 structure, resulting in asymmetric 4- and 5-membered rings around 3-coordinated SA and symmetric two 6-membered rings around 4-coordinated SA.

Although all of the TM atoms within 3d-5d range can serve as central site for SA structures, Tc, Cd, and Hg are ruled out from consideration due to their toxicity and radioactivity.[34] Accordingly, a total of 26 TM atoms (Figure 1b) are chosen to generate 78 E-TM-N_x-C structures for screening ORR/OER bifunctional catalysts. Most of the E-TM-N_x-C structures retain their stable geometries during structural relaxation. Exception is Zr, Ru, Ta in E-TM-N_3-C together with Ta in E-TM-N_2-C, and these unstable configurations are not considered in our current work. The structural parameters of the 74 optimized stable E-TM-N_x-C structures are presented in Table S1, and the average bond length of TM-N ranges from 1.75 Å (E-Co-N_2-C) to 2.49 Å (E-Y-N_3-C). Interestingly, due to the high symmetry of both E-TM-N_2-C and E-TM-N_4-C models, these geometries exhibit reflectional symmetries after structural relaxation. More specifically, with the TM single atom as the symmetry axis, the values of the TM-N_x bond lengths (d_{TM-Nx}) on both sides are exactly the same ($d_{TM-N1} = d_{TM-N2}$ in E-TM-N_2-C, and $d_{TM-N1} = d_{TM-N3}$, $d_{TM-N2} = d_{TM-N4}$ in E-TM-N_4-C). As for asymmetrical E-TM-N_3-C structures, the TM center tends to move toward the edges of the graphene nanoribbon, and three TM-N bonds have a tendency to average out in these structures. Moreover, the embedded TM atoms in some E-TM-N_4-C moieties protrude out of the planar configurations after structural relaxation. Setting 1 Å as the structure protrusion threshold, we found that Sc, Y, Zr, Nb, Mo, Hf, W and Re are off the plane of the E-TM-N_4-C structures (Table S2). These TM atoms all belong to the IIIB-VIIB groups with large atomic radiuses. At the same time, the E-TM-N_4-C structures exhibit a higher TM-N coordination number compared with E-TM-N_2-C and E-TM-N_3-C. Accordingly, the central TM atoms with large atom radiuses are hindered from moving in the plane for E-TM-N_4-C structures, instead they tend to protrude off the planes. Hence, both the central TM atom radius and the coordination environment influence the final structure of E-TM-N_x-C system.

High structural stability is the prerequisite for a catalytic structure.[35] Accordingly, the formation energy (E_f) together with the dissolution potential (U_{diss}) of E-TM-N_x-C structures are calculated to determine the thermodynamic and electrochemical stabilities.[35-36] From the E_f *vs.*

U_{diss} plots depicted in Figure 1c-1e (values are provided in Table S3-S5), the coordinate plane can be divided into four quadrants, corresponding to different levels of structural stabilities. According to the definition of E_f and U_{diss}, the T_1 region with $E_f < 0$ eV and $U_{diss} > 0$ V is considered to be thermodynamically and electrochemically stable, and these materials should be feasible for experimental synthesis and characterization.

The E-TM-N_2-C, E-TM-N_3-C and E-TM-N_4-C are classified through the above stability criteria. For E-TM-N_2-C structures, the corresponding E_f all exhibit positive values. Additionally, only Au and Os exhibit positive U_{diss} on E-TM-N_2-C substrates. The above results indicate that the binding between the TM atoms and N species are quite weak in such structures, and that they may not be experimentally feasible. In the case of E-TM-N_3-C, except for Mo, W, Re, and Os atoms, other central sites could reach a negative E_f value, leading to thermodynamically stable structures. However, 8 structures are examined to have negative U_{diss} among these thermodynamically stable E-TM-N_3-C structures, demonstrating that the metal species (Sc, Ti, V, Cr, Mn, Y, Nb and Hf) in E-TM-N_3-C moieties might dissolve into the electrolyte under the electrochemical conditions. Intriguingly, most of the unstable structures (in T_2 and T_4 quadrants) are constructed by early transition metals with larger atomic radii. These species generally form relatively long bonds with adjacent N species (1.97 Å - 2.27 Å in E-TM-N_3-C). This will lead to a rather weak interaction between central metal site and substrate, resulting in structural instability. Although E-Ag-N_3-C and E-Au-N_3-C exhibit rather long average TM-N bonds, 2.16 and 2.12 Å, respectively, both of these structures show negative E_f and positive U_{diss}, indicating both thermodynamic and electrochemical stabilities. It can be inferred from above analysis that the structural stability of E-TM-N_3-C is also determined by the TM species, while the TM-N bond length is not a sufficient condition for evaluating structural stability.

Unlike E-TM-N_2-C, all the E-TM-N_4-C structures exhibit acceptable thermodynamic stabilities ($E_f < 0$). Additionally, 3 structures containing early transition metals (Y, Zr, and Hf) fall in the electrochemically unstable T_4 quadrant with relatively large atomic radii, which is similar to E-TM-N_3-C. It should be noted that these three structures have TM-protruding structures as mentioned before (Table S2), indicating that such configuration may reduce the structural stabilities of E-TM-N_4-C. Figure 1f shows the mapping structural stabilities for E-TM-N_2-C, E-TM-N_3-C and E-TM-N_4-C. One can see that, as the coordination number of TM-N increases, the structural configurations tend to become stable, and the saturated TM-N_4 structures are beneficial

for stabilizing transition metal central sites both thermodynamically and electrochemically. To sum up, based on the stability screening process, 11 of E-TM-N_3-C structures and 23 of E-TM-N_4-C structures have been identified for OER/ORR catalytic investigations.

2.2. Tendency of ORR/OER activities for E-TM-N_x-C

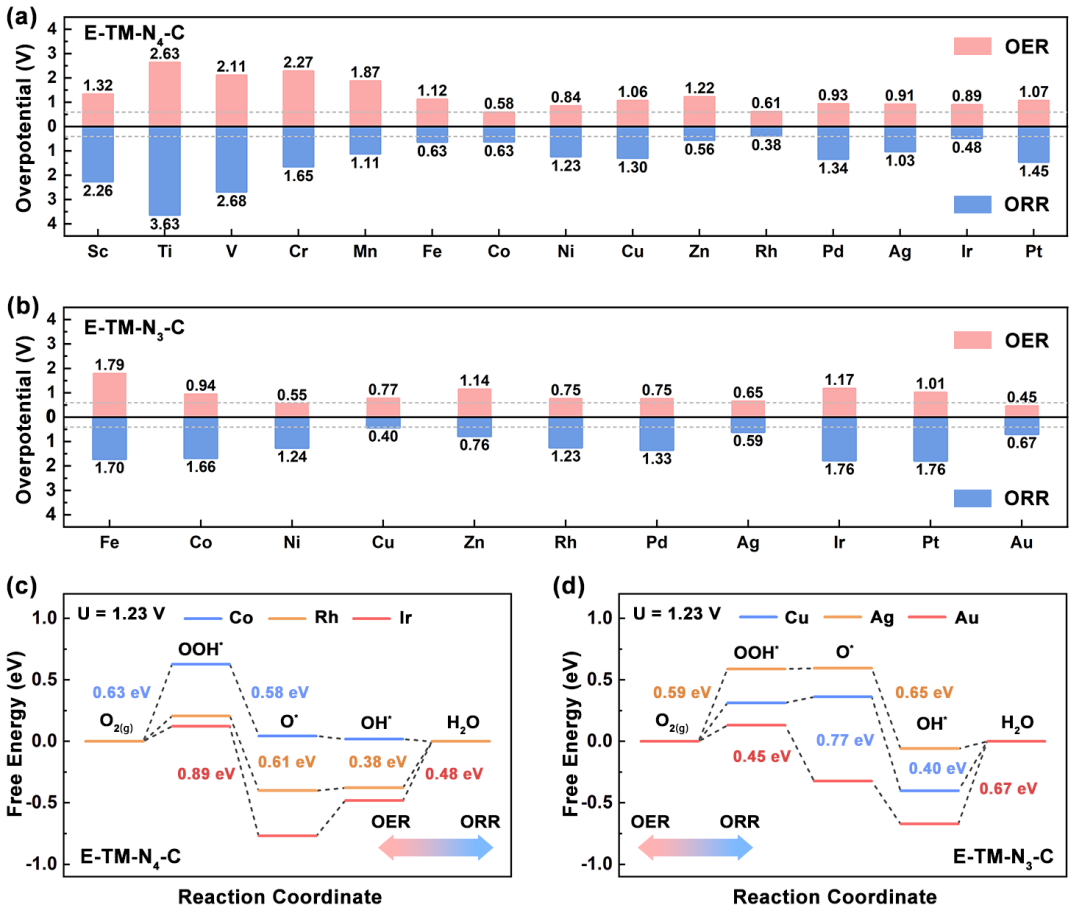

Figure 2. Screening of E-TM-N_x-C catalysts for oxygen reactions. The oxygen bifunctional reaction overpotentials of (a) E-TM-N_4-C and (b) E-TM-N_3-C. The horizontal dashed lines represent the overpotential of 0.41 V for Pt (111) at ORR region and the overpotential of 0.59 V for IrO_2 (110) at OER region. The free energy diagrams of ORR/OER on (c) E-TM-N_4-C (TM = Co, Rh, Ir) and (d) E-TM-N_3-C (TM = Cu, Ag, Au) under U = 1.23 V.

Subsequently, the ORR/OER activities of the 34 E-TM-N_x-C structures are screened from stability results. The classical adsorbate evolution mechanism (AEM) of ORR/OER is considered in this work, which includes the adsorption of three oxygen-containing intermediates (OOH*, O*,

and OH*).[37] More specifically, in the ORR process, the first step involves the adsorption of O_2 molecules and proton-electron pair ($H^+ + e^-$) on the active sites (TM) of E-TM-N_x-C, resulting in the formation of OOH*. In the second step, the generated OOH* reacts with another proton-electron pair to form O*, while releasing H_2O. Then, the third proton-electron pair combines with O* to form the third intermediate, OH*. The fourth step involves the combination of OH* with proton-electron pair to form H_2O molecule and desorption, thus restoring the catalyst adsorption sites to their initial state. Accordingly, the overall reaction steps of OER are the reverse of the ORR. As the state-of-art catalytic structures, the Pt (111) facet and the IrO_2 (110) facet were chosen as benchmarks for ORR and OER, respectively. Based on our calculation conditions, the theoretical overpotentials are η_{ORR} = 0.41 V for Pt (111) and η_{OER} = 0.59 V for IrO_2 (110), which is similar with previous results.[7,38] Based on the free energy diagrams (Figure S1, Table S6), Pt (111) binds the OOH* relatively weak, and the formation of OOH* becomes the potential-determining step (PDS) during ORR. As for IrO_2 (110), the interaction between Ir active sites and *OOH is slightly strong, leading to the PDS fall in the OOH* desorption step. Next, the catalytic performances of the E-TM-N_x-C structures are analyzed. According to the obtained adsorption energies of the three oxygen-containing intermediates (Table S7 and Figure S2), the adsorption energies show an obvious trend of $\Delta G_{OOH*} > \Delta G_{O*} > \Delta G_{OH*}$ for both E-TM-N_4-C and E-TM-N_3-C, indicating potential scaling relations among these three intermediates. Additionally, it should be noted that on some E-TM-N_4-C (TM = Nb, Mo, Ru, Ta, W, Re, Os, Au) structures, O* and OOH* adsorbates cannot maintain their original configurations, so the corresponding ΔG_{O*} and ΔG_{OOH*} values were not computed. Hence, we choose ΔG_{OH*} to analyze the adsorption trends of different metals. As present in Figure S3, the adsorption strength of OH gradually decreases for most 3d, 4d, and 5d TMs as their radius decreases, demonstrating a periodic behavior. Moreover, E-TM-N_4-C always exhibit a positive ΔG_{OH*} compared with E-TM-N_3-C, indicating a weaker adsorption derived from structural features.

The ORR and OER overpotentials for E-TM-N_4-C and E-TM-N_3-C are computed (Figure 2a, 2b and Table S8, S9), respectively. In case of ORR, 9 structures exhibit promising overpotentials less than 1 V. These promising ORR catalytic structures follow a trend of E-Rh-N_4-C (0.38 V) < E-Cu-N_3-C (0.40 V) < E-Ir-N_4-C (0.48 V) < E-Zn-N_4-C (0.56 V) < E-Ag-N_3-C (0.59 V) < E-Fe-N_4-C (0.63 V) = E-Co-N_4-C (0.63 V) < E-Au-N_3-C (0.67 V) < E-Zn-N_3-C (0.76 V). Notably, both E-Rh-N_4-C and E-Cu-N_3-C exhibit comparable ORR activities to Pt (111) facet among these

structures. As for OER, there are 12 structures possessing overpotentials below 1 V. Specially, 6 of E-TM-N_4-C structures (Co, Rh, Ni, Ir, Ag and Pd) achieve relatively small theoretical overpotentials of 0.58, 0.61, 0.84, 0.89, 0.91, and 0.93 V, respectively. The Au, Ni, Ag, Pd, Rh, Cu, and Co SAs in E-TM-N_3-C structure show overpotentials of 0.45, 0.55, 0.65, 0.75, 0.75, 0.77 and 0.94 V, respectively. Hence, the E-Co-N_4-C, E-Au-N_3-C and E-Ni-N_3-C are considered as efficient OER catalytic structures that are even better than IrO_2 (110) facet.

The relationship between ΔG_{OH^*} and ORR/OER overpotentials for E-TM-N_x-C are investigated. Intriguingly, some structures with large overpotentials of ORR/OER ($\eta_{ORR/OER}$ > 1 V) always exhibit strong interaction with OH* intermediates (ΔG_{OH^*} < -0.4 eV), including Sc, Ti, V, Cr SAs in E-TM-N_4-C and Fe, Co, Ir, Pt SAs in E-TM-N_3-C. As presented in Figure S4 and S5, these structures usually have potential determining step (PDS) at the OH*desorption step for ORR and the OOH*desorption step for OER. Similar conclusions can be drawn by comparing the E-TM-N_4-C and E-TM-N_3-C structures. As a trend, the catalytic activity of E-TM-N_4-C generally exceeds that of E-TM-N_3-C due to moderate OH* adsorption.

The reaction process of some SA structures with potential bifunctional properties ($\eta_{ORR/OER}$ < 1 V) are summarized (Figure 2c and 2d), including Co, Rh, Ir SAs in E-TM-N_4-C and Cu, Ag, Au SAs in E-TM-N_3-C. Notably, by judging the possible PDS for both ORR and OER, all these structures exhibit a PDS at the OOH* formation step or the OH* desorption step for ORR. As for OER, either the O* formation step or the OOH* formation step is determined to be PDS. Among these structures, E-Rh-N_4-C exhibits the lowest theoretical overpotential for ORR (η_{ORR} = 0.38 V) and a small theoretical overpotential for OER (η_{OER} = 0.61 V), which is comparable to Pt (111) (η_{ORR} = 0.41 V) and IrO_2 (110) (η_{OER} = 0.59 V), respectively. The above screening results conclude that the E-Rh-N_4-C stand out as an efficient bifunctional catalytic structure for both ORR and OER among all E-TM-N_x-C structures.

To demonstrate the structural advantages of E-SACs, we select the E-TM-N_x-Cs with promising catalytic activities for OER and/or ORR, as summarized before, and construct the corresponding in-plane pyridinic TM-N_4 structures (labelled as C-TM-N_4-C, where the first C denotes 'centred') for comparison (Figure S6 and S7). As for ORR, except for Zn and Co SAs, the E-TM-N_x-C activities are significantly enhanced compared with C-TM-N_4-C structures. Specifically, Cu, Ag, Au, and Ir species show reduced ORR overpotential by 0.7, 0.6, 0.58, and 0.61 V, respectively. Our E-Fe-N_4-C structure also outperforms the C-Fe-N_4-C structure,

consistent with previous experiment result.[23] In case of OER, for most SAs, including Au, Ni, Ag, Pd, Cu, and Ir, the E-TM-N_x-Cs demonstrate superior catalytic activities to C-TM-N_4-C. For example, the overpotentials are reduced by 0.75 and 0.53 V for Au and Ni species, respectively. This comparison supports our speculation that the unsaturated edge sites can effectively influence the adsorption strength of catalytic intermediates, thereby endowing E-SACs with enhanced catalytic activities.

Considering that the electroreduction of O_2 can generate H_2O through the 4-eletron pathway or generate H_2O_2 through the 2-eletron pathway, it is necessary to evaluate the ORR selectivity on E-TM-N_x-C. Upon OOH* formation ($* + O_2 + H^+ + e^- \rightarrow OOH^*$), in the 4-eletron pathway, OOH* proceeds to form H_2O through $OOH^* + H^+ + e^- \rightarrow O^* + H_2O$; while in the 2-eletron pathway, $OOH^* + H^+ + e^- \rightarrow H_2O_2$ occurs. Hence, if ΔG_{O^*} on E-TM-N_x-C is less than 3.52 eV ($\Delta G_{H2O2} - \Delta G_{H2O}$), the catalytic structure thermodynamically favors H_2O formation following the 4-eletron pathway.[35] We summarize the ΔG_{O^*} values on E-TM-N_x-C, as shown in Figure S8. The results indicate that most E-TM-N_3-C and E-TM-N_4-C structures exhibit a strong adsorption of O* with ΔG_{O^*} less than 3.52 eV, suggesting better selectivity towards H_2O rather than H_2O_2 formation. Specifically, 28 E-TM-N_x-C structures exhibit a 4-eletron pathway selectivity, and the affinity for O* intermediate of TM active sites gradually diminishes through a periodic behavior, consistent with the previously discussed OH* adsorption. This could be attributed to the gradual increase in d-electrons of TM atoms within the same period, resulting in the filling of anti-bonding states of the TM-O bond and thereby weakening the adsorption strength for O*. Additionally, five E-TM-N_4-C structures (TM = Ni, Cu, Zn, Pd, and Pt) exhibit relatively weak adsorption of O*, resulting in a preference for H_2O_2 formation.

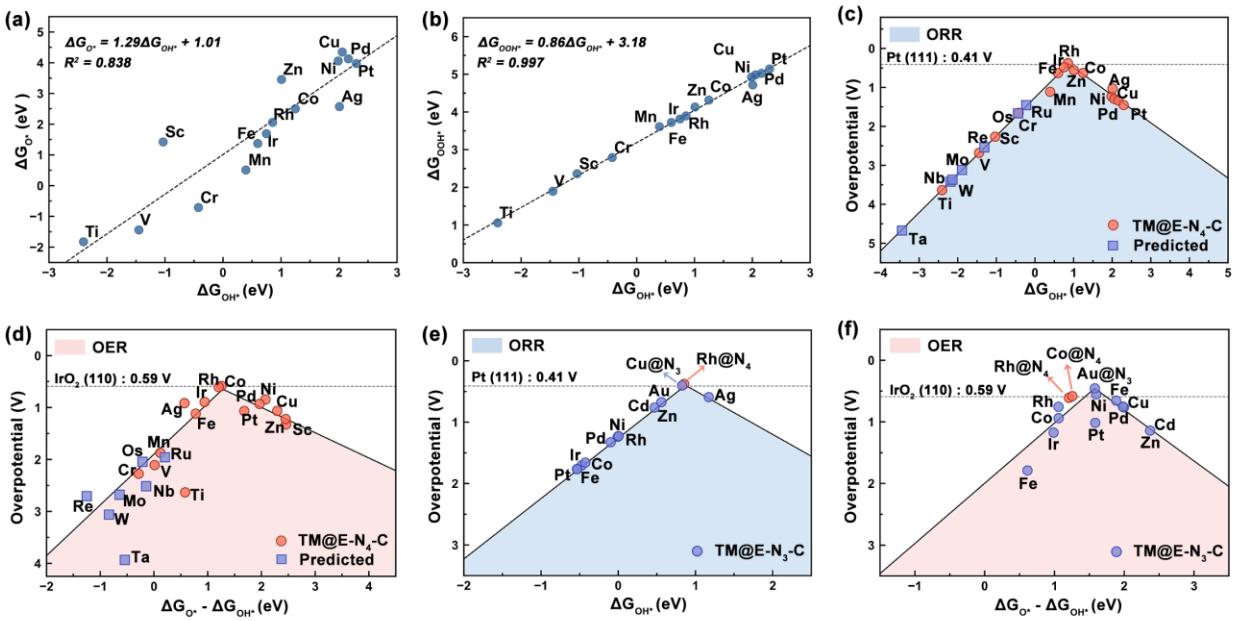

Figure 3. Scaling relationships and volcano plots. Adsorption free energies of intermediates: (a) ΔG_{OH^*} *vs.* ΔG_{O^*} and (b) ΔG_{OH^*} *vs.* ΔG_{OOH^*} on E-TM-N_4-C. The lines are linear fitting to computed data. The volcano plots of (c) ΔG_{OH^*} *vs.* η_{ORR} and (d) ΔG_{O^*}-ΔG_{OH^*} *vs.* η_{OER} on E-TM-N_4-C. The predicted overpotentials (blue squares) are also included into the volcano plots. The volcano plots of (e) ΔG_{OH^*} *vs.* η_{ORR} and (f) ΔG_{O^*}-ΔG_{OH^*} *vs.* η_{OER} on E-TM-N_3-C.

The deep relationships among the three O-containing intermediates are evaluated. Based on the above adsorption energy results of OH*, O* and OOH* (Table S7 and Figure S2), there could exist linear correlations between these intermediates. Nørskov et al. reported that scaling relations can be observed among OH*, O* and OOH* for metal and metal oxide systems.[39-40] However, it remains unclear if the scaling relation can be extended to edge-anchored single atom systems. Accordingly, the linear regression method is used to fit the relationships in E-TM-N_x-C structures (Figure 3a, 3b and Figure S9). The relationships of ΔG_{O^*} and ΔG_{OOH^*} with ΔG_{OH^*} for E-TM-N_4-C can be linear fitted as follows,

$$\Delta G_{O^*} = 1.29 \times \Delta G_{OH^*} + 1.01 \quad (R^2 = 0.838) \tag{1}$$

$$\Delta G_{OOH^*} = 0.86 \times \Delta G_{OH^*} + 3.18 \quad (R^2 = 0.997) \tag{2}$$

Notably, a strong linear correlation between the two variables can be achieved when the R^2 value is close to 1. The above fitting results confirm the linear correlation in E-TM-N_4-C. Similar conclusion can be drawn for E-TM-N_3-C. As presented in Figure S9, the values of R^2 are calculated

to be 0.848 and 0.925 for ΔG_{OH*} *vs.* ΔG_{O*} and ΔG_{OH*} *vs.* ΔG_{OOH*}, respectively. Hence, we may conclude that the E-SAC systems also follow the scaling relation for three O-containing intermediates, and the as-obtained ΔG_{OH*} can be used to derive the value of ΔG_{O*} and ΔG_{OOH*}.

Then, for analyzing the catalytic activity trends of E-TM-N_x-C structures, the ΔG_{OH*} and ΔG_{O*}-ΔG_{OH*} are selected as descriptors to construct the volcano plots for ORR and OER, respectively.[41] Some ΔG_{OOH*} values that cannot be computed through DFT calculations are derived from their ΔG_{OH*} based on the above linear equations (Table S7). The as-predicted ORR/OER overpotentials are provided on the volcano plots (blue squares). The free energy diagrams of ORR/OER for all E-TM-N_x-C structures are presented in Figure S4 and S5 for evaluating the specific catalytic processes for ORR/OER. According to the Sabatier's principle, neither strong nor weak interactions for adsorbates are favorable for catalytic reaction.[42] Typically, the catalysts located at the top of volcano plot exhibit optimal bonding strengths for catalytic intermediates, leading to a high intrinsic catalytic activity. In case of ORR for E-TM-N_4-C system (Figure 3c), structures located on the left side of the volcano mainly involve the PDS of $OH^* + H^+ + e^- \rightarrow * + H_2O$ (except for E-Mn-N_4-C), indicating stronger bonding with OH* for SA site. Conversely, some structures (SA = Co, Ni, Cu, Pd, Ag, Pt) with more positive ΔG_{OH*} (weaker adsorption for OH*) is located on the right side, and the PDS is primarily $* + O_2 + H^+ + e^- \rightarrow OOH^*$. Notably, E-Rh-$N_4$-C is located at the top of the volcano plot, signifying its superior ORR activity among all E-TM-N_4-C systems, with an optimal ΔG_{OH*} of 0.85 eV. As for the ORR volcano plot for E-TM-N_3-C (Figure 3e), except for E-Ag-N_3-C, the remaining E-TM-N_3-C structures are situated on the left side of the ORR volcano plot, indicating strong adsorption with OH* compared with E-TM-N_4-C, consistent with our previous analysis. E-Cu-N_3-C is located at the top of the ORR volcano plot, with an overpotential of 0.40 eV for ORR, accompanied by an optimal ΔG_{OH*} of 0.83 eV.

As for OER volcano plot of E-TM-N_4-C (Figure 3d), 13 structures are located on the left leg of the volcano, with the primary PDS being $O^* + H_2O \rightarrow OOH^* + H^+ + e^-$, indicating strong adsorption with oxygen intermediates. 6 structures are situated on the right side of the volcano, and the PDS are evaluated to be mainly $OH^* \rightarrow O^* + H^+ + e^-$ and $H_2O \rightarrow OH^* + H^+ + e^-$, suggesting relatively weak bonding with intermediates. Both E-Co-N_4-C and E-Rh-N_4-C are positioned at the top of the OER volcano plot, indicating their optimal OER activity compared to other structures. For the E-TM-N_3-C structures (Figure 3f), E-Au-N_3-C and E-Ni-N_3-C are located at the top of the

volcano plot, suggesting moderate adsorptions for all three intermediates towards OER. From the volcano plots of all 41 E-TM-N_x-C structures, E-Rh-N_4-C has been identified as a favorable structure for bifunctional ORR/OER catalysis.

2.3. Evaluating the activity and stability of E-TM-N_x-C under reaction condition

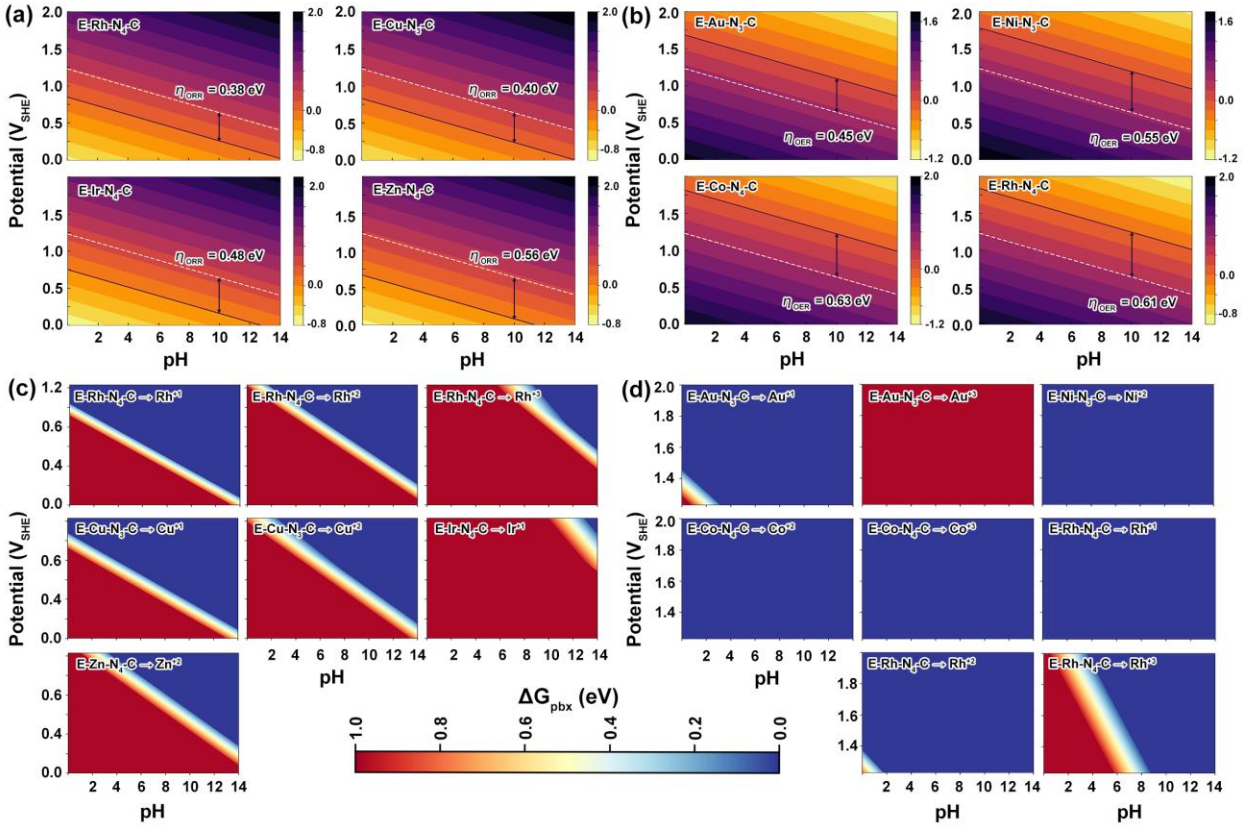

Figure 4. The impacts of potential and pH on the catalytic activity and stability of the most active E-TM-N_x-C. (a) The activity plot and (c) the stability plot of E-Rh-N_4-C, E-Cu-N_3-C, E-Ir-N_4-C and E-Zn-N_4-C under ORR condition. (b) The activity plot and (d) the stability plot of E-Au-N_3-C, E-Ni-N_3-C, E-Co-N_4-C and E-Rh-N_4-C under OER condition. The white dashed line in the activity plot (a, b) represents the theoretic equilibrium state for ORR/OER. The black lines denote the reaction free energy value with 0 eV, the boundary condition for catalytic reaction. The blue region in the stability plot (c, d) denotes the E-TM-N_x-C would be favorable for ORR/OER rather than aqueous dissolution.

The influence of potential and pH values under ORR/OER condition on catalytic behavior for the most active E-TM-N_x-C structures is subsequently evaluated. For the ORR, the E-Rh-N_4-C, E-Cu-N_3-C, E-Ir-N_4-C and E-Zn-N_4-C are selected as they are the top four ORR catalysts among E-TM-N_x-C. In the case of OER, the top four active structures are E-Au-N_3-C, E-Ni-N_3-C, E-Co-N_4-C and E-Rh-N_4-C. As for activity plots, the potential and pH values are introduced to build potential- and pH-dependent ORR/OER reaction free energy diagrams covering a potential range of 0 to 2 V and a pH range of 0 to 14. As shown in Figure 4a and 4b, when the reaction free energy value is less than 0 eV, it indicates the spontaneous occurrence of ORR/OER. Accordingly, a reaction free energy value with 0 eV represents the boundary condition for catalytic reaction (denoted by black lines). As for ORR in Figure 4a, the catalytic active area always resides in the lower left corner, demonstrating that lower potentials and lower pH values are favorable for ORR, while the OER process behaves oppositely (Figure 4b). Additionally, the ORR/OER overpotential values obtained from the activity plots for E-TM-N_x-C are consistent align with our preceding calculations, indicating that both ORR and OER overpotentials in the present mechanism are insensitive to pH, which is also consistent with related research by Nørskov and co-workers.[7]

The catalytic stabilities of the above E-TM-N_x-C structures are studied following a similar method in Nørskov's work.[43] Specifically, the free energies for demetallation reaction of E-TM-N_x-C under reaction condition are calculated through Eq (3),

$$C_xN_yM + mH^+ \rightleftharpoons C_xN_yH_m + M^q + (q-m)e^- \quad (3)$$

which represents the hydrogenation of the N atoms for E-SACs under the demetallation mechanism. In this equation, m denotes the number of adsorbed H atoms, and q represents the charges of the solvated metal ions. Accordingly, the Pourbaix stability of E-TM-N_x-C can be determined based on the demetallation free energies at different potentials *vs.* SHE and varying pH, and the potential range is set as 0 to 1.23 V for ORR (Figure 4c) and 1.23 to 2 V for OER (Figure 4d). Among the E-TM-N_x-C with promising ORR activities, all four structures can maintain their structural stability under strong alkaline and high potential conditions (blue regions in Figure 4c); However, metal atoms tend to dissolve from the E-TM-N_x-C under strong acidic and low potential conditions (red regions in Figure 4c). More specifically, the Rh-N_4-C, E-Cu-N_3-C and E-Zn-N_4-C are relatively stable at pH=14, and the metal dissolution potential is smaller than the ORR onset potential, illustrating that these three structures can catalyze ORR reaction before dissolution occurs. In contrast, the E-Ir-N_4-C has an opposite trend; It tends to undergo metal

dissolution rather than ORR even under pH 14 condition, indicating that E-Ir-N_4-C is unstable under ORR condition. In case of OER, except for E-Au-N_3-C, which cannot maintain structural stability under all pH conditions, the other three structures are highly stable. E-Rh-N_4-C exhibits a stability region beyond pH 8, whereas E-Ni-N_3-C and E-Co-N_4-C are stable under both acidic and alkaline conditions. To sum up, although most E-TM-N_x-C can maintain structural stability in certain pH range, their ORR stability needs to be further enhanced to meet application requirements by, for example, xxxx.

Since some studies show that the solvation effect may affect the binding strength between the reaction intermediates and the surfaces, thereby influencing the predicted catalytic activities.[44] The solvation effect is incorporated in the DFT calculations, and the calculated ORR/OER overpotentials with and without considering solvation effects are summarized in Figure S10 and S11 for E-TM-N_4-C and E-TM-N_3-C, respectively. Although the solvation effect influences the absolute values of the calculated overpotentials, it has minimal influence on the relative activity order of the screened E-SACs, which is consistent with previous studies.[45] Therefore, for simplicity, the solvation effect is not further considered in this work.

2.4. Identifying the activity origin of E-Rh-N_4-C

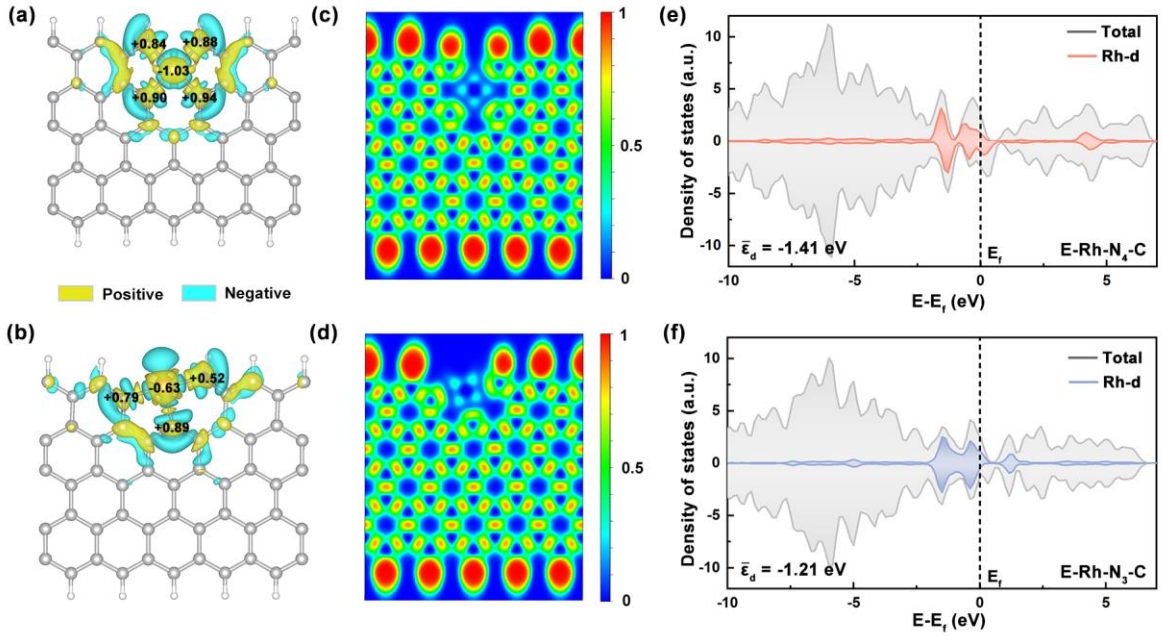

Figure 5. Surface electronic structure calculations of E-Rh-N_4-C and E-Rh-N_3-C. The charge density difference of (a) E-Rh-N_4-C and (b) E-Rh-N_3-C. The yellow and blue regions represent

electron accumulation and depletion, respectively. The plots of electron location function for (c) E-Rh-N_4-C and (d) E-Rh-N_3-C. Projected density of states of Rh d orbitals and total density of states for (e) E-Rh-N_4-C and (f) E-Rh-N_3-C.

The electronic structure of E-Rh-N_4-C is evaluated to identify the origin of its bifunction catalytic activity. Considering the structural similarity, E-Rh-N_3-C is also studied as a reference. The charge density difference together with the Bader charge analysis is performed to examine the charge transfer process between Rh SA and N species for E-TM-N_x-C structures (Figure 5a and 5b). Specifically, in E-Rh-N_4-C, the Rh SA transfers 1.03 electrons to the surrounding N atoms, while in E-Rh-N_3-C, the total electron transfer from Rh to N is computed to be 0.63. These results indicate that the saturated N coordination of E-Rh-N_4-C leads to a greater electron transfer compared with the E-Rh-N_3-C counterpart. Such a stronger electron exchange between Rh SA and coordinated nitrogen species is supported by the electron localization function (ELF). As shown in Figure 5c and 5d, an electron delocalization around Rh SA can be observed for both E-Rh-N_4-C and E-Rh-N_3-C, indicating the formation of ionic bonds between the Rh SA and N species. Comparatively, E-Rh-N_4-C exhibits a lower accumulation of electrons around the Rh SA, indicating a greater charge transfer from Rh to the neighboring N atoms, which is consistent with the above analysis. Subsequently, the density of states (DOS) is calculated to show how the Rh-N coordination environment influences the electronic structure of Rh SA. Figure 5e and 5f show that E-Rh-N_4-C exhibits higher DOS at the Fermi level compared to E-Rh-N_3-C. The Rh average d-band centers are computed to be -1.41 and -1.21 eV for E-Rh-N_4-C and E-Rh-N_3-C, respectively. A more positive d-band center will lead to a stronger interaction with intermediates according to the d-band center theory.[46] This comparison interprets the adsorption difference of O-containing adsorbates for E-Rh-N_4-C and E-Rh-N_3-C.

The electronic structures of E-Rh-N_4-C and E-Rh-N_3-C with O-containing adsorbates are analyzed. Figure 6a and Figure S12 presents the stable adsorption configurations for E-Rh-N_4-C and E-Rh-N_3-C, respectively. The E-Rh-N_4-C exhibits longer Rh-O bond lengths compared with E-Rh-N_3-C, indicating weaker bonded states with these adsorbates. Additionally, Figure 6b shows the charge transfer values from E-Rh-N_x-C to O-containing intermediates based on Bader charge analysis. Together with the charge density difference plots, all the O-containing adsorbates obtain less electrons from E-Rh-N_4-C than from E-Rh-N_3-C, demonstrating relatively weak electron

interactions. The Rh-O binding strengths for E-Rh-N_4-C and E-Rh-N_3-C are confirmed by the projected density of states (pDOS) and the crystal orbital Hamilton populations (COHPs) for the intermediate-adsorbed structures. The overlap between the Rh d orbitals and the O p orbitals in E-Rh-N_4-C is lower than that in E-Rh-N_3-C (Figure 6c and Figure S13), indicating a relatively weaker orbital hybridization behavior of E-Rh-N_4-C compared with E-Rh-N_3-C. Moreover, compared to E-Rh-N_3-C, the antibonding orbitals of Rh-O in E-Rh-N_4-C move lower towards the Fermi level (Figure 6d), which would weaken the bonding state for Rh-O bonds. The above conclusion is supported by the value of integrated crystal orbital Hamilton populations (ICOHPs) (Table S10), which is more positive for E-Rh-N_4-C.

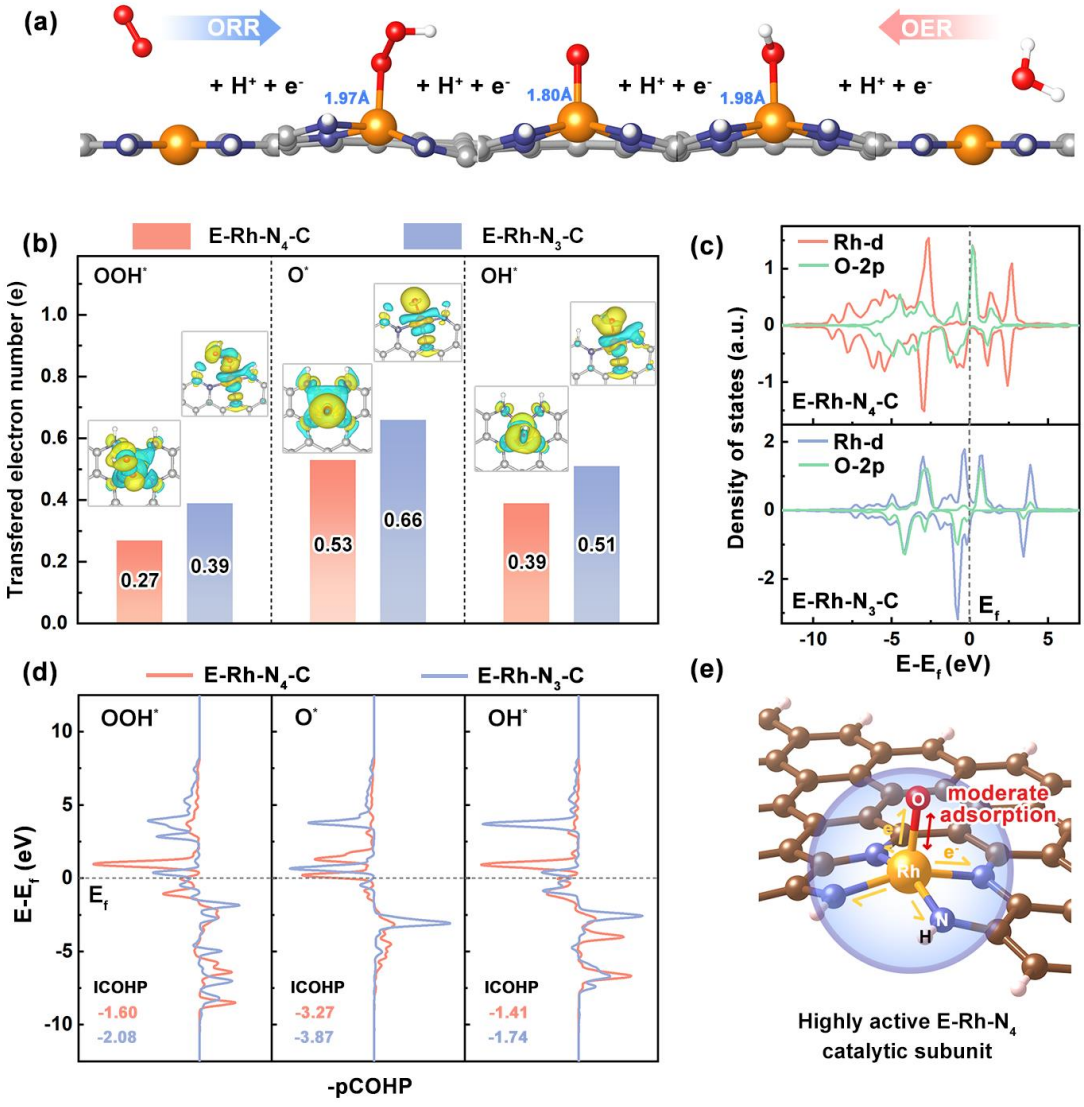

Figure 6. Mechanism analysis for identifying highly active E-Rh-N_4 catalytic subunit. (a) Optimized E-Rh-N_4-C structures for 4-electron ORR/OER processes with Rh atoms serving as adsorption sites. (b) The values of charge transferred from E-Rh-N_4-C (red)/E-Rh-N_3-C (blue) to OOH*, O* and OH* based on Bader charge analysis, together with the corresponding charge density difference plots. (c) The PDOS of Rh d orbitals and O p orbitals for E-Rh-N_4-C (up)/E-Rh-N_3-C (down) after O* adsorption. (d) The COHP of Rh-O bonds for OOH-adsorbed, O-adsorbed and OH-adsorbed E-Rh-N_4-C (red)/E-Rh-N_3-C (blue). (e) Schematic of E-Rh-N_4 catalytic subunit accelerating the oxygen reaction through moderate O* adsorption.

Detailed catalytic processes are analyzed through the free energy diagrams for E-Rh-N_4-C (Figure 2c) and E-Rh-N_3-C (Figure S5f), respectively. In case of ORR, the PDS for both E-Rh-N_4-C and E-Rh-N_3-C involve the desorption of OH*, indicating strong adsorption of OH* on both surfaces. As for OER, both E-Rh-N_4-C and E-Rh-N_3-C follow the same PDS, which are determined to be the transition step from O* to OOH*. Hence, for both OER and ORR, the E-Rh-N_x-C structures perform similar catalytic mechanisms; which all originate from relatively strong interaction with the O-containing adsorbates. However, E-Rh-N_4-C exhibit smaller overpotentials of 0.38 and 0.61 V for ORR and OER, respectively. The promotion mechanism of E-Rh-N_4-C is present in Figure 6e. The saturated N coordination environment transfers a significant portion of electrons from the Rh SA to the O-containing intermediates, which in turn influences the d orbitals of Rh sites. Comparing to E-Rh-N_3-C, the Rh SA in E-Rh-N_4-C provide fewer electrons to the adsorbed O-containing intermediates, leading to a relatively weak interaction that benefits both ORR and OER process. Additionally, these results also indicate that both heteroatoms and vacancy structures can be introduced into the E-TM-N_x-C structures to tune the intrinsic catalytic activity of TM SA sites, constructing ideal bifunctional catalytic architectures.

To confirm the distinct structures of edge-anchored SACs, the electronic structures of E-Rh-N_4-C and C-Rh-N_4-C are compared. Although C-Rh-N_4-C shares a similar first coordination shell structure with E-Rh-N_4-C (Figure S6), E-Rh-N_4-C exhibits asymmetric charge distributions due to edge effect (Figure 5a). Notably, the Rh site in E-Rh-N_4-C loses more electrons than that in C-Rh-N_4-C, while the N species gain fewer electrons (Figure S14). Additionally, in contrast to C-Rh-N_4-C, where all four N atoms exhibit similar electron transfer numbers, the two N atoms further away from the edge in E-Rh-N_4-C gain more electrons, and similar phenomenon can be

observed from E-Rh-N_3-C. Accordingly, a portion of the electrons transferred to N species should originate from the C sites connected to N, which belong to the second coordination shell of Rh SAs. The SAs locate at edge sites would lead to fewer connections between N and C, resulting in fewer transferred electrons for N pattern. As for Rh SAs, N in C-Rh-N_4-C can obtain a considerable number of electrons from adjacent C, hence Rh SAs will transfer relatively fewer electrons to maintain the structural stability. In summary, the Rh SAs at edge site construct a specific second coordination shell for E-SACs, which substantially impacts the electronic structure of Rh SAs and coordinated N species.

The d-band centers (ε_d) of TM and the p-band centers (ε_p) of N of the C-TM-N_4-C structures are compared with the corresponding E-TM-N_4-C and E-TM-N_3-C structures (Figure S15) to determine the effect of coordinated patterns and edge configurations on electronic structure regulation for TM and N species. The ε_d of TM SAs show similar trends for both spin-up and spin-down states, except for Fe, Co, and Ru, which exhibit significant spin polarizations. Additionally, the value of ε_d in E-TM-N_3-C exhibit more pronounced difference compared to E-TM-N_4-C and C-TM-N_4-C, indicating that the coordination structure has a greater impact on the electronic structures of TM SAs than edge effects. While for ε_p of N species, the trends for both spin-up and spin-down are the same, as there is no polarization effect for N. As the variations of ε_p for the three SAC structures do not exhibit a similar trend, it suggests that both edge sites and coordination structures play a substantial role in influencing the electronic structure of N. This analysis verifies the contribution of edge sites at second coordination shell in modulating the catalytic activities of E-SACs.

2.4. Training ML models to describe E-TM-N_x-C

Although high-throughput DFT calculations allow us to screen potential catalytic active structures based on current E-TM-N_x-C structures, it is necessary to explore other catalytic structures and establish design principles. For this purpose, we intend to build a correlation between the inherent structural features and the intrinsic catalytic activities for universal edge-anchored single atom graphene structures. To this end, the relationship between ε_d and ΔG_{OH^*} for E-TM-N_x-C structures has been carefully investigated. As illustrated in Figure S16, weak correlations ($R^2 < 0.31$) between ε_d and ΔG_{OH^*} are observed for both E-TM-N_4-C and E-TM-N_3-

C structures, indicating that while ε_d is a widely adopted descriptor,[47] it is not sufficiently accurate for describing ΔG_{OH^*} in edge-anchored single atom graphene systems.

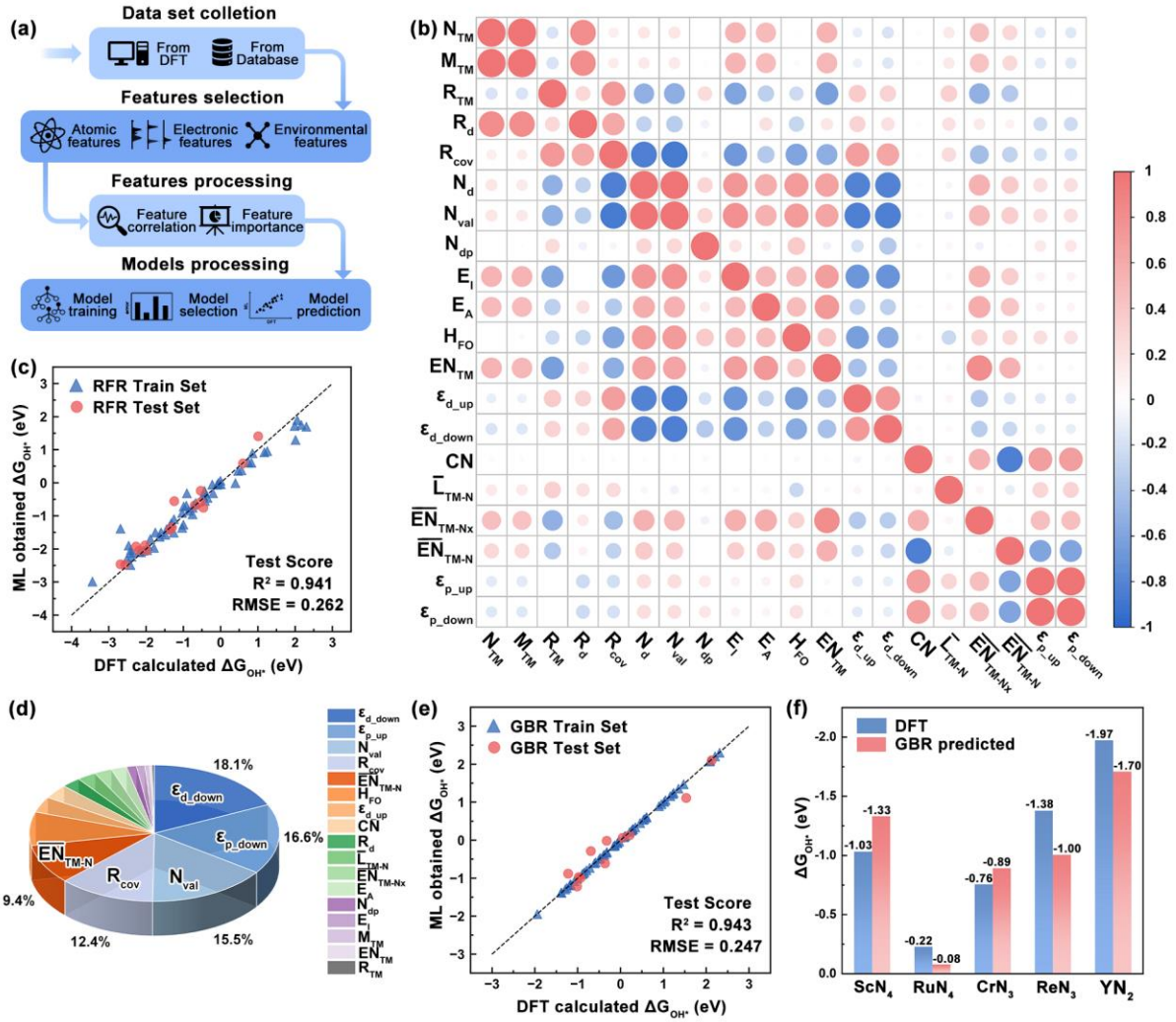

Figure 7. Introduction of ML for the E-TM-N$_x$-C structures. (a) Workflow of involved ML investigations. (b) Pearson correlation plots of 20 features for E-SACs. (c) DFT calculated ΔG_{OH^*} *vs* ML predicted ΔG_{OH^*} from the RFR model. (d) Feature importance of the 17 features with the corresponding proportion. (e) DFT calculated ΔG_{OH^*} *vs* ML predicted ΔG_{OH^*} from the GBR model. (f) Comparison of DFT and GBR predicted ΔG_{OH^*} values for 5 extra structures.

Consequently, we turn to machine learning (ML) methods to explore the relationship between various descriptors and catalytic activity[48-50] in order to construct an effective model to describe the ΔG_{OH^*} of E-TM-N$_x$-C structures. The overall ML workflow is illustrated in Figure 7a. To build the ML training database, the ΔG_{OH^*} values for the 74 E-TM-N$_x$-C structures (including those with

positive E_f and negative U_{diss}) are collected. Additionally, a total of 20 input features are considered[51], as summarized in Table S11, which includes atomic features, electronic structure features, and environmental structural features. To be more specific, (i) the atomic features, such as the atomic mass (M_{TM}), atomic radius (R_{TM}) and covalent radius (R_{cov}), characterize the physical properties of the TM atoms. These data can be obtained from literature or handbooks. (ii) The electronic structure features describe the electronic properties of the TM SA in E-TM-N_x-C structures, including the adjusted electron numbers of d/p orbital (N_{dp}), the number of d electrons (N_d), and the d-band center (ε_{d_up} and ε_{d_down}), which are commonly closely correlated with catalytic activity. (iii) The environmental structural features, including the SA coordination number (CN), the average electronegativity of the TM-N bond ($\overline{EN}_{TM-N}$), and the N p-band center (ε_{p_up} and ε_{p_down}), capture the local structure and electronic structure of the TM SA together with its coordination environment in E-TM-N_x-C structures. To improve the training efficiency and minimize the prediction bias, a process of dimensionality reduction was performed through removing the features which have high feature-feature correlation. As shown in Figure 7b, by calculating the Pearson correlation coefficients (PCC) among the feature dataset, we have identified strong correlations (PCC > 0.9) between pairs such as N_{TM} *vs.* M_{TM}, N_d *vs.* N_{val}, and ε_{p_up} *vs.* ε_{p_down}. Accordingly, three features including N_{TM}, N_{val} and ε_{p_up} are removed, resulting in a reduced input set comprising 17 features.

Considering the constraints of our limited dataset, a random forest regressor (RFR) model was chosen for training.[52] The R^2 values for the training and test sets were determined to be 0.952 and 0.941, respectively (Figure 7c), with RMSE values of 0.297 and 0.262, indicating the effectiveness of the RFR model. Given that key features could offer valuable insights into the internal factors of catalytic structures for governing catalytic activity, the feature importance was evaluated based on the RFR model. Figure 7d illustrates the top five ranked features and proportions: ε_{d_down} (18.1%), ε_{p_down} (16.6%), N_{val} (15.5%), R_{cov} (12.4%), and $\overline{EN}_{TM-N}$ (9.4%). The cumulative feature importance exceeds 70%. Hence, the catalytic activities of E-TM-N_x-C are dominantly determined by the electronic properties of TM SAs and coordinated N species. Considering that edge sites can effectively affect the electronic structures of TM and N, as evidenced by the above electronic structure analysis, we may conclude that the combined interaction of the edge effects, N patterns and TM SAs collectively govern the intrinsic catalytic activities. In other words, the TM SA at edge sites in E-TM-N_x-C structures interacts with the

neighboring coordinating species to form a specific catalytic subunit, which will dominantly influence the catalytic activity.

Additionally, a gradient boosting regression (GBR) model is also trained to achieve higher accuracy for predicting the E-TM-N_x-C structures. Differing from the RFR model, a subset comprising ΔG_{OH*} values and corresponding features for 5 structures is randomly dropped from the dataset, which serve as a series of input variables for the final GBR model. This results in a dataset size of 69*17 for training the GBR model. The high linearity presented in Figure 7e suggests the reliability of our GBR model in predicting relevant structures.[53] We then applied our GBR model to predict the ΔG_{OH*} values for as-mentioned subset, in comparison to the DFT-calculated values (Figure 7f). Although some deviations can be observed between two values with a maximum difference of 0.38 eV, it should be noted that these five structures are actually 'unfamiliar' to the GBR model. Consequently, the catalytic activities of edge-anchored single atom graphene systems can be estimated based on our GBR model together with the linear functions for scaling relation, which has significant implications for the rational design of efficient electrocatalysts.

3. Conclusion

Edge-anchored single-atom catalysts as a kind of promising catalytic structures are carefully considered in this work. A set of 78 E-SACs with different N coordination patterns are investigated through high-throughput calculation together with machine learning. By screening thermodynamically and electrochemically stable structures, we have identified that E-Au-N_3-C, E-Ni-N_3-C, and E-Co-N_4-C are efficient OER catalysts, while E-Cu-N_3-C is ORR favorable, and E-Rh-N_4-C is the best candidate for OER/ORR bifunctionality. A relatively strong scaling relationship among O-containing intermediates has been identified in E-SACs, and the as-derived volcano plots further strengthen the above findings. For most catalytic active E-TM-N_x-C structures, both activities and stabilities are studied under ORR/OER conditions with contribution of pH and potential. Moreover, the electronic structure analysis accompanied by the machine learning results prove that edge effects together with coordinated patterns significantly impacts the electronic structure of TM SAs and N species through the "TM-N-C" atomic configuration. Hence, the TM atoms, coordinated species, and various edge sites in E-SACs cooperatively construct the specific catalytic subunit. As the subunit serves as the basis for the intrinsic catalytic activity,

altering the edge configurations, constructing defect sites or introducing other coordinated species are effective routes for catalytic performance enhancement. Finally, we have demonstrated that our as-trained GBR model, together with the linear functions of scaling relation, can effectively predict the catalytic activities of E-SACs. This work may inspire data-driven investigations for expanding the design of E-SACs on other platforms such as semiconducting 2D materials.

Acknowledgements. This work was supported by the National Natural Science Foundation of China (Grant No. 22369003, Grant No. 52001306 and Grant No. 22005116) and the specific research fund of the Innovation Platform for Academicians of Hainan Province (YSPTZX202123), Hainan Provincial Natural Science Foundation of China (Grant No. 223QN185), Scientific Research Starting Foundation of Hainan University (Grant No. KYQD(ZR)-22022), and the Collaborative Innovation Center project of Hainan University (XTCX2022XXB01).

References

[1] S. Chu, A. Majumdar, *Nature* **2012**, 488, 294.
[2] Z. Shi, J. Li, Y. Wang, S. Liu, J. Zhu, J. Yang, X. Wang, J. Ni, Z. Jiang, L. Zhang, Y. Wang, C. Liu, W. Xing, J. Ge, *Nat. Commun.* **2023**, 14, 843.
[3] S. S. Shinde, C. H. Lee, J.-Y. Jung, N. K. Wagh, S.-H. Kim, D.-H. Kim, C. Lin, S. U. Lee, J.-H. Lee, *Energy Environ. Sci.* **2019**, 12, 727.
[4] Z.-F. Huang, J. Wang, Y. Peng, C.-Y. Jung, A. Fisher, X. Wang, *Adv. Energy Mater.* **2017**, 7.
[5] D. Guo, R. Shibuya, C. Akiba, S. Saji, T. Kondo, J. Nakamura, *Science* **2016**, 351, 361.
[6] Y. L. Zhang, K. Goh, L. Zhao, X. L. Sui, X. F. Gong, J. J. Cai, Q. Y. Zhou, H. D. Zhang, L. Li, F. R. Kong, D. M. Gu, Z. B. Wang, *Nanoscale* **2020**, 12, 21534.
[7] I. C. Man, H. Y. Su, F. Calle‐Vallejo, H. A. Hansen, J. I. Martínez, N. G. Inoglu, J. Kitchin, T. F. Jaramillo, J. K. Nørskov, J. Rossmeisl, *ChemCatChem* **2011**, 3, 1159.
[8] D. S. Gnanamuthu, J. V. Petrocelli, *J. Electrochem. Soc.* **1967**, 114.
[9] S. Trasatti, *Electrochim. Acta* **1984**, 29, 1503.
[10] M. Luo, M. T. M. Koper, *Nat. Catal.* **2022**, 5, 615.
[11] Y. Yu, J. Zhou, Z. Sun, *Adv. Funct. Mater.* **2020**, 30.
[12] X. Liang, K.-X. Zhang, Y.-C. Shen, K. Sun, L. Shi, H. Chen, K.-Y. Zheng, X.-X. Zou, *J. Electrochem.* **2022**, 28, 2214004.
[13] Y.-P. L. Tao Zhang, Qi-Tong Ye, Hong-Jin Fan, *J. Electrochem.* **2022**, 28, 2214006.
[14] J. Quílez‐Bermejo, S. García‐Dalí, A. Daouli, A. Zitolo, R. L. S. Canevesi, M. Emo, M. T. Izquierdo, M. Badawi, A. Celzard, V. Fierro, *Adv. Funct. Mater.* **2023**, 33.
[15] J. Balamurugan, P. M. Austeria, J. B. Kim, E. S. Jeong, H. H. Huang, D. H. Kim, N. Koratkar, S. O. Kim, *Adv. Mater.* **2023**, 35.
[16] P. Zhang, K. Chen, J. Li, M. Wang, M. Li, Y. Liu, Y. Pan, *Adv. Mater.* **2023**, 35.
[17] M. Wang, W. Yang, X. Li, Y. Xu, L. Zheng, C. Su, B. Liu, *ACS Energy Lett.* **2021**, 6, 379.

[18] Z. Wang, X. Jin, R. Xu, Z. Yang, S. Ma, T. Yan, C. Zhu, J. Fang, Y. Liu, S.-J. Hwang, Z. Pan, H. J. Fan, *ACS Nano* **2023**, 17, 8622.
[19] H. Yang, S. Gao, D. Rao, X. Yan, *Energy Stor. Mater.* **2022**, 46, 553.
[20] Q. Li, W. Chen, H. Xiao, Y. Gong, Z. Li, L. Zheng, X. Zheng, W. Yan, W. C. Cheong, R. Shen, N. Fu, L. Gu, Z. Zhuang, C. Chen, D. Wang, Q. Peng, J. Li, Y. Li, *Adv. Mater.* **2018**, 30, e1800588.
[21] L. Yang, D. Cheng, H. Xu, X. Zeng, X. Wan, J. Shui, Z. Xiang, D. Cao, *Proc. Natl. Acad. Sci. U.S.A.* **2018**, 115, 6626.
[22] K. Zhao, X. Nie, H. Wang, S. Chen, X. Quan, H. Yu, W. Choi, G. Zhang, B. Kim, J. G. Chen, *Nat. Commun.* **2020**, 11, 2455.
[23] X. Wang, Y. Jia, X. Mao, D. Liu, W. He, J. Li, J. Liu, X. Yan, J. Chen, L. Song, A. Du, X. Yao, *Adv. Mater.* **2020**, 32, e2000966.
[24] Y. Zhao, W. J. Jiang, J. Zhang, E. C. Lovell, R. Amal, Z. Han, X. Lu, *Adv. Mater.* **2021**, 33, e2102801.
[25] Q. Wang, Y. Tan, S. Tang, W. Liu, Y. Zhang, X. Xiong, Y. Lei, *ACS Nano* **2023**, 17, 9565.
[26] H. Zhang, W. Zhou, X. F. Lu, T. Chen, X. W. Lou, *Adv. Energy Mater.* **2020**, 10.
[27] Y. Tian, M. Li, Z. Wu, Q. Sun, D. Yuan, B. Johannessen, L. Xu, Y. Wang, Y. Dou, H. Zhao, S. Zhang, *Angew. Chem. Int. Ed.* **2022**, 61, e202213296.
[28] M. Xiao, Z. Xing, Z. Jin, C. Liu, J. Ge, J. Zhu, Y. Wang, X. Zhao, Z. Chen, *Adv. Mater.* **2020**, 32, e2004900.
[29] Z. Zhang, Y. Chen, L. Zhou, C. Chen, Z. Han, B. Zhang, Q. Wu, L. Yang, L. Du, Y. Bu, P. Wang, X. Wang, H. Yang, Z. Hu, *Nat. Commun.* **2019**, 10, 1657.
[30] Y. Cheng, S. Zhao, H. Li, S. He, J.-P. Veder, B. Johannessen, J. Xiao, S. Lu, J. Pan, M. F. Chisholm, S.-Z. Yang, C. Liu, J. G. Chen, S. P. Jiang, *Appl. Catal. B* **2019**, 243, 294.
[31] M. Ha, D. Y. Kim, M. Umer, V. Gladkikh, C. W. Myung, K. S. Kim, *Energy Environ. Sci.* **2021**, 14, 3455.
[32] P. Yang, J. Li, D. G. Vlachos, S. Caratzoulas, *Angew. Chem. Int. Ed.* **2023**, DOI: 10.1002/anie.202311174e202311174.
[33] L.-H. Xu, W. Liu, K. Liu, *Adv. Funct. Mater.* **2023**, n/a, 2304468.
[34] L. Zhang, X. Guo, S. Zhang, S. Huang, *J. Mater. Chem. A* **2022**, 10, 11600.
[35] X. Guo, S. Lin, J. Gu, S. Zhang, Z. Chen, S. Huang, *ACS Catal.* **2019**, 9, 11042.
[36] J. Greeley, J. K. Nørskov, *Electrochim. Acta* **2007**, 52, 5829.
[37] H. Jin, C. Guo, X. Liu, J. Liu, A. Vasileff, Y. Jiao, Y. Zheng, S. Z. Qiao, *Chem. Rev.* **2018**, 118, 6337.
[38] J. K. Nørskov, J. Rossmeisl, A. Logadottir, L. Lindqvist, J. R. Kitchin, T. Bligaard, H. Jónsson, *J. Phys. Chem. B* **2004**, 108, 17886.
[39] J. Rossmeisl, A. Logadottir, J. K. Nørskov, *Chem. Phys.* **2005**, 319, 178.
[40] J. Rossmeisl, Z. W. Qu, H. Zhu, G. J. Kroes, J. K. Nørskov, *J. Electroanal. Chem.* **2007**, 607, 83.
[41] A. Kulkarni, S. Siahrostami, A. Patel, J. K. Nørskov, *Chem. Rev.* **2018**, 118, 2302.
[42] M. Gajdo, A. Eichler, J. Hafner, *J. Phys. Condens. Matter* **2004**, 16, 1141.
[43] N. Karmodak, J. K. Nørskov, *Angew. Chem. Int. Ed.* **2023**, 62.
[44] X. Zhao, Y. Liu, *J. Am. Chem. Soc.* **2021**, 143, 9423.
[45] H. Xu, D. Cheng, D. Cao, X. C. Zeng, *Nat. Catal.* **2018**, 1, 339.
[46] B. Hammer, J. K. Norskov, *Nature* **1995**, 376, 238.
[47] J. Liu, W. Luo, L. Wang, J. Zhang, X.-Z. Fu, J.-L. Luo, *Adv. Funct. Mater.* **2022**, 32, 2110748.

[48] K. S. Exner, *Mater. Today Energy* **2023**, 36.
[49] J. Ren, X. Lin, J. Liu, T. Han, Z. Wang, H. Zhang, J. Li, *Mater. Today Energy* **2020**, 18.
[50] J. Y. Lok, W.-H. Tsai, I. C. Cheng, *Mater. Today Energy* **2023**, 36.
[51] Y. Chen, H. Cui, Q. Jiang, X. Bai, P. Shan, Z. Jia, S. Lu, P. Song, R. Feng, Q. Kang, Z. Liang, H. Yuan, *ACS Appl. Nano Mater.* **2023**, 6, 7694.
[52] R. Diaz-Uriarte, S. Alvarez de Andres, *BMC Bioinform.* **2006**, 7, 3.
[53] X. Liu, Y. Zhang, W. Wang, Y. Chen, W. Xiao, T. Liu, Z. Zhong, Z. Luo, Z. Ding, Z. Zhang, *ACS Appl. Mater. Interfaces* **2022**, 14, 1249.